

Article

Cascaded H-Bridge Multilevel Converter Applied to a Wind Energy Conversion System with Open-End Winding

Samuel dos Santos Bettoni ^{*}, Herbert de Oliveira Ramos , Frederico F. Matos  and Victor Flores Mendes ^{*}

Graduate Program in Electrical Engineering, Federal University of Minas Gerais, Belo Horizonte 31270-901, Brazil; herbert-ramos11@ufmg.br (H.d.O.R.); fredmatos@ufmg.br (F.F.M.)

^{*} Correspondence: sbettoni@ufmg.br (S.d.S.B.); victormendes@cpdee.ufmg.br (V.F.M.)

Abstract: With the growing expansion of renewable sources around the world, wind energy is among those that stand out. With the advances of technology, wind turbine projects have considerably increased their power, reaching higher power, mainly for offshore installations. One of the main challenges is the power converters, more specifically the semiconductor components, which have limited voltage and current capabilities. Thus, the concept of multilevel converters emerged, increasing the voltage levels and thus carrying higher power levels. In addition to the application of multilevel converters, it is possible to increase the voltage and power levels employing an open-end winding (OEW) connection to the generator. In this context, the present work investigated the application of a multilevel converter (three-level cascaded H-bridge back-to-back) driving a squirrel-cage induction machine in an open-end winding configuration, connected to a wind energy conversion system (WECS). The analysis of the proposed system was developed through dynamic simulation of a 1.67 MW WECS, using PLECS software, including the modeling of the main system components: generator, power converters, system control, filter, and grid connection. The results show that the objective of obtaining a 5-level behavior in the output voltage is achieved by using the OEW connection. Furthermore, a low harmonic content is achieved in the machine current as in the current injected into the grid. In addition, it is possible to verify the power distribution between the converters, demonstrating that converters with smaller power can be combined to reach higher WECS power.

Keywords: multilevel converter; open-end winding; wind energy; distributed generated; squirrel-cage induction machine



Citation: Bettoni, S.d.S.; Ramos, H.d.O.; Matos, F.F.; Mendes, V.F. Cascaded H-Bridge Multilevel Converter Applied to a Wind Energy Conversion System with Open-End Winding. *Wind* **2023**, *3*, 232–252. <https://doi.org/10.3390/wind3020014>

Academic Editor: Zhe Chen

Received: 3 March 2023

Revised: 6 April 2023

Accepted: 4 May 2023

Published: 9 May 2023



Copyright: © 2023 by the authors. Licensee MDPI, Basel, Switzerland. This article is an open access article distributed under the terms and conditions of the Creative Commons Attribution (CC BY) license (<https://creativecommons.org/licenses/by/4.0/>).

1. Introduction

In the last years, the expansion of renewable energy sources has increased around the world; the significant increase in photovoltaic and wind systems has especially stood out. In terms of wind generation, the expectation is that new installations around the world will remain high in the coming years, as shown in Figure 1, in the study carried out by the Global Wind Energy Council (GWEC) and the International Energy Agency (IEA). Reflecting this, the expected annual growth in new installations is 6.6% [1,2]. Each year, offshore installations have become a way to expand wind generation. From 2018 to 2021 (Figure 1), there was an increase of more than 30 GW in the total installed capacity offshore, which represents about 7% of the total installed capacity of the wind energy conversion system. This was a highlight for the year 2021, which was best year in terms of new offshore installations.

With the increase in the power of wind turbines, especially when referring to offshore installation, power converters operate in the boundary limits of voltage and current. Thus, several works were developed in order to allow the converters to operate at higher voltage levels, with special attention to multilevel converters [3–6]. Multilevel converters are topologies composed of combinations of power semiconductor devices, connected together and controlled in such a way that they produce, in the output, a voltage waveform with

multiple steps of amplitude. These output voltage waveforms depend on the number of converter levels, consequently increasing the output voltage, even when using the same semiconductors previously used in traditional converters. Higher voltage levels are reached, allowing them to be connected to high-power generators without compromising the electrical limits of semiconductors, and also with advantages for the filter project and output energy quality. Several multilevel topologies were developed, as Neutral Point Clamped (NPC) [7], Flying Capacitor (FC) [8,9], and the Cascaded H-Bridge (CHB) [10,11].

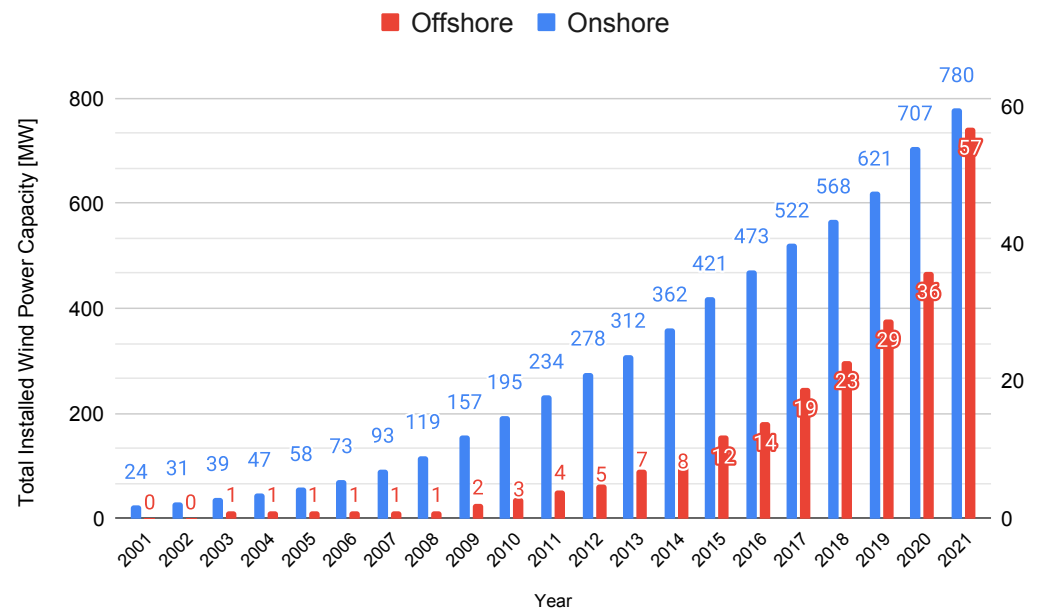


Figure 1. Evolution of wind energy around the world [1].

In this work, CHB topology was investigated, which has similar behavior to the NPC, but it does not present an unequal loss distribution, nor the clamped diodes [12]. Among the advantages of using the CHB multilevel converter, the following can be mentioned: greater efficiency; uniform losses in switching components [13]; modularity; fault tolerance—as it is possible to operate the system with reduced power even if there is a failure in any of the components of the IGBT-diode pairs of the power converter (redundancy in the state of switching) [5]; a smaller number of components when compared to the NPC and FC [14]; and, finally, it does not present the capacitor voltage balancing problem that occurs in the NPC and FC topologies [4]. One of the disadvantages of the full bridge converter and, consequently, of the CHB, is the necessity of isolated DC buses, that is, it must be independent for each cell of the H-bridge converter [6].

Another possibility to obtain a multilevel voltage behavior at the terminals of an electric machine is employing an open-end winding (OEW) connection [15]. In an OEW configuration, the machine terminals are not connected in delta or star, so the six machine terminals (for a three phase system) are available to be connected by power converters. Several applications were proposed using this open windings topology: electrical vehicles [16], photovoltaic-fed water-pump drive systems [17], motor drives with nine-level inverters using conventional three-phase two-level voltage source inverters (2L-VSC) and CHB [18], motor drives with six-level inverters using a cascade of two 2L-VSC and a single 2L-VSC [19], and wind systems [20].

Considering the application of multilevel converters and open-end winding in wind energy conversion systems (WECS), several works proposed different topologies: three-phase two-level converters arranged back-to-back [21], neutral point clamped converters [22], diode full-bridge rectifiers with an NPC inverter [23], and flying capacitor converters [24].

There is still a lack of studies that evaluate the wind energy conversion system using a CHB multilevel converter in open-end windings drives. Therefore, this work aimed to

investigate the use of three-level H-bridge converters in a cascade, which will result in a behavior of a five-level voltage output.

The main contribution of this work resides in the topology of a CHB multilevel converter (back-to-back 3L-HB) used to drive a machine in an open-end windings configuration. In several applications, the grid side of the CHB back-to-back converter consists of a three-phase full-bridge diode rectifier or a 2L-VSC [25]. For this reason, in this work, the great contribution was the back-to-back topology using a 3L-HB converter on both sides. For this purpose, a wind energy conversion system was simulated using an induction machine with a squirrel cage operating with an open-end winding generator. The simulations were developed using PLECS[®] software and considering a 1.67 MW WECS.

The structure of this article is organized as follows: Section 2 presents a theoretical foundation whose main theme is dealing with the concept of a multilevel converter and the topology of machines with open-end winding. In Section 3, the application of using the five-level converter driving machines with OEW and the control techniques used in the proposed system are presented. In Section 4, the proposed system was simulated and the results obtained. Section 5 presents the conclusions and future works.

2. System Description

2.1. Wind Energy Conversion System

The function of a wind energy conversion system is to transform the kinetic energy of the wind (captured through wind turbines) into electrical energy to be injected into the electrical grid, as shown in Figure 2. In this work, emphasis was given to the electrical subsystem, more specifically to the power electronic converter (multilevel converter) and the electric generator (Squirrel Cage Induction Generator—SCIG). Power converters are responsible for making this energy flow effective and reliable [26,27].

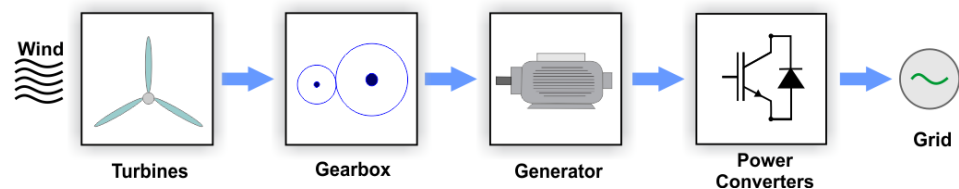


Figure 2. Basic configuration of a WECS.

When considering the power extracted from the wind by the turbine, the efficiency of this conversion is called the power coefficient, C_p , that is, the ratio between the turbine power and the wind power, which is defined by:

$$C_p = \frac{P_{turbine}}{P_{wind}}. \quad (1)$$

Thus, the mechanical power converter by a wind turbine is given by the following equation:

$$P_{turbine} = \frac{1}{2} \rho \pi r^2 C_p(\lambda, \beta) V_w^3, \quad (2)$$

where ρ is the air density, r is the radius of the swept area of rotor blades, and V_w is the wind speed.

The power coefficient is dependent on two important variables, the pitch angle β and the tip speed ratio (λ), defined as:

$$\lambda = \frac{\omega_t r}{V_w} \quad (3)$$

where ω_t is the turbine rotational speed.

In order to obtain the maximum extraction of wind power from a variation in wind speed, it is necessary for the wind generator to operate with variable rotor speed in order to

obtain an optimal tip speed ratio ($\lambda_{optimal}$), i.e., a value that results in the maximum value of C_p . In this work, pitch angle control was not considered, since its objective is just power limitation, so β was kept at zero.

2.2. Generator

In this work, the dynamic equations of the machine will be used in the synchronous reference frame, so the dynamic equations of the machine become [28]:

$$v_{sd} = R_s i_{sd} + p \lambda_{sd} - \omega_{sf} \lambda_{sq} \quad (4)$$

$$v_{sq} = R_s i_{sq} + p \lambda_{sq} + \omega_{sf} \lambda_{sd} \quad (5)$$

$$v_{rd} = R_r i_{rd} + p \lambda_{rd} - (\omega_{sf} - \omega_e) \lambda_{rq} \quad (6)$$

$$v_{rq} = R_r i_{rq} + p \lambda_{rq} + (\omega_{sf} - \omega_e) \lambda_{rd} \quad (7)$$

$$\lambda_{sd} = L_s i_{sd} + L_m i_{rd} \quad ; \quad \lambda_{sq} = L_s i_{sq} + L_m i_{rq} \quad (8)$$

$$\lambda_{rd} = L_r i_{rd} + L_m i_{sd} \quad ; \quad \lambda_{rq} = L_r i_{rq} + L_m i_{sq}, \quad (9)$$

where p refers to d/dt and the indices d and q to the direct and quadrature axis, respectively; the other indices s and r refer to the stator and rotor, respectively; v_s and v_r are voltages; R_s and R_r are winding resistances; λ_s and λ_r are flux linkages; i_s and i_r are currents; the variable L refers to the self-inductance; L_m is the magnetization inductance; ω_{sf} the speed of the rotating frame; and finally, ω_e the speed, in electrical radians, of the machine.

For this work, it was considered an orientation of the d -axis of the rotating frame dq in the rotor flux, thus,

$$\lambda_{rq} = 0. \quad (10)$$

The power of the machine can be obtained by:

$$P_e = \frac{3}{2} (v_{sd} i_{sd} + v_{sq} i_{sq} + v_{rd} i_{rd} + v_{rq} i_{rq}). \quad (11)$$

However, for the squirrel-cage induction machine, the terms $v_{rd} = v_{rq} = 0$. Substituting these null terms and the terms v_{sd} and v_{sq} , expressed in the Equations (4), and (5) in Equation (11):

$$P_e = \frac{3}{2} \omega_e L_m (i_{sq} i_{rd} - i_{sd} i_{rq}). \quad (12)$$

The electromagnetic torque developed in the machine can be obtained by dividing Equation (12) by the mechanical speed of the machine, and with the orientation in the rotor flux ($\lambda_{rq} = 0$):

$$T_e = \frac{3 P L_m}{2 L_r} (\lambda_{rd} i_{sq}), \quad (13)$$

where P is the number of poles in the machine.

2.3. Multilevel Converter and Electric Machines with Open-End Windings

As previously mentioned, by increasing the power of wind turbines, conventional converters operate at their electrical limits. Multilevel converters and machine drives with OEW are employed to reduce the individual power of the converters, also increasing the voltage level of the arrangement [29].

In a CHB multilevel converter, the number of resulting levels, per phase, at the output of this arrangement are given by $2n + 1$, where n is the number of full bridge converter (cells). Thus, a five-level converter, as employed in this work, needs two cells per phase to reach this number of levels [6]. Figure 3a shows a schematic of cell connection to obtain

a five-level CHB converter. In the same figure, Figure 3b, the waveform of the outputs of each full-bridge cell and the CHB arrangement is represented, where the five levels in the output phase voltage can be seen.

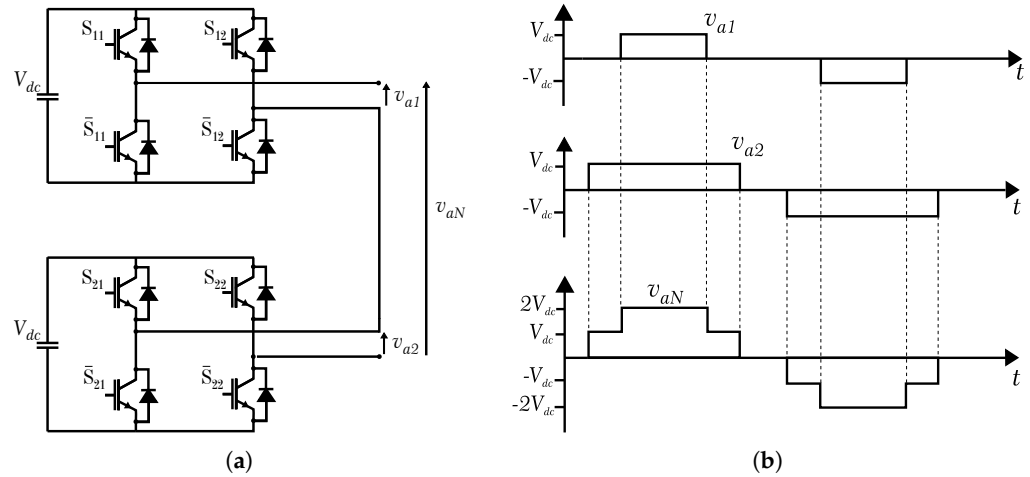


Figure 3. CHB multilevel converter. (a) Structure of five-level CHB multilevel converter. (b) Waveforms of the output voltage of the individual H-bridges (v_{a1} and v_{a2}) and the CHB arrangement (v_{aN}).

Considering the phase A, the output phase voltage equation of the CHB converter shown in Figure 3 is defined as:

$$v_{aN} = v_{a1} + v_{a2}, \tag{14}$$

where v_{a1} and v_{a2} are the output phase voltage of the top cell and bottom cell, respectively.

Given that the command signals from switching devices are defined as $S_{ij} \in \{1, 0\}$ where i and $j \in \{1, 2\}$ and \bar{S}_{ij} are the complementary, thus Equation (14) can be written as a function of the command signals and the DC bus voltage. For example, the CHB of Figure 3a can be described by:

$$v_{aN} = (S_{12} - S_{11})V_{dc} + (S_{21} - S_{22})V_{dc}. \tag{15}$$

Table 1 shows the output voltage values when using the CHB, according to the topology of Figure 3a.

As can be seen in Table 1, the output voltage of the CHB shown in Figure 3 has five-level voltage: $-2V_{dc}$, $-V_{dc}$, 0 , V_{dc} and $2V_{dc}$. It is also possible to verify that the maximum output voltage is obtained when the two DC sources are connected in series, resulting in the output value of $2V_{dc}$ instead of V_{dc} .

In each cell of the CHB converter, there are $2^2 = 4$ possible switching states and, based on the same reasoning, in each phase of the CHB multilevel converter (Figure 3 and Table 1), there are $2^2 \cdot 2^2 = 16$ possible switching states per phase. Considering the three phases of the system, then there will be $2^{12} = 4096$ possible switching states in this CHB multilevel converter under study. Among these switching states, there are several redundant states, which become an advantage of the topology, since a certain output voltage is obtained with several possibilities in the switching state of the switches. From the Table 1, it can be seen that the V_{dc} output voltage is obtained by four different combinations of switch states.

Table 1. Output Phase Voltage and Switching States.

Switching States				Output Voltage (Phase A)
S_{11}	S_{12}	S_{21}	S_{22}	v_{aN}
1	0	1	0	$2V_{dc}$
0	0	1	0	V_{dc}
1	0	0	0	
1	0	1	1	
1	1	1	0	
0	0	0	0	0
0	0	1	1	
0	1	1	0	
1	0	0	1	
1	1	0	0	
1	1	1	1	
0	0	0	1	
0	1	0	0	$-V_{dc}$
0	1	1	1	
1	1	0	1	
0	1	0	1	$-2V_{dc}$

Operating the machine with OEW, it helps to obtain high voltage levels in high power applications [15]. In this type of drive, the machine windings are neither star- nor delta-connected, as in a traditional drive but, instead, the six machine terminals are connected by different converters at each end of the windings [21]. In Figure 4, a general schematic of an electric machine drive with open-end windings is shown.

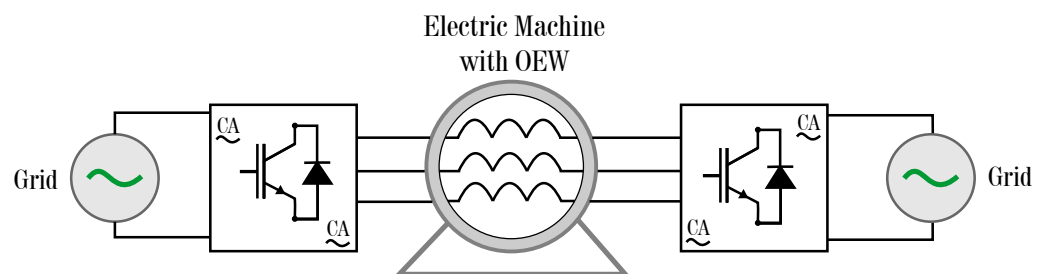


Figure 4. Generic drive of a machine with open-end windings.

Using the advantage of an OEW drive and also using multilevel converters, the number of voltage levels at the machine terminals can be further increased. For example, if three-level converters are used to drive a machine with OEW, the waveform of the synthesized voltages is equivalent to a five-level converter, which consequently increases the redundancy in the switching states [30]. The redundancy in the switching states is useful for the development of optimized switching patterns and also it is possible to continue the operation with the failure of some semiconductors.

3. Proposed System

In this work, six full-bridge converters on the machine side (*Machine Side Converter—MSC*) and six on the grid side (*Grid Side Converter—GSC*) were employed, connected in such a way that they reproduced a CHB multilevel converter. In Figure 5, a schematic is presented representing the proposed structure.

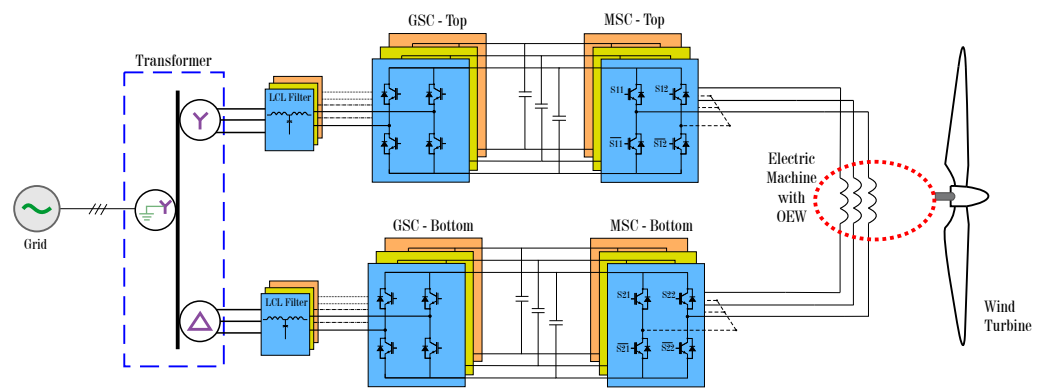


Figure 5. WECS with CHB five-level back-to-back converters (MSC and GSC) driving an asynchronous generator with open-end windings.

The MSCs were controlled to maximize the power extracted from the wind, making the generator operate with variable speed. The grid-side converters were used to control the voltages on the DC-links and also to control the injection of reactive power into the grid.

As shown in Figure 5, the system was fed by a transformer that had two secondary windings because, as previously mentioned, each full-bridge cell on the grid side must be connected by an independent voltage, as they need independent DC-links. In addition, the inherent characteristic of the CHB multilevel converter require that the phases are isolated from each other [12]. This structure has the disadvantage of having more converters, but the total power is divided among them, thus the power of each one is a fraction of the generator power and, consequently, semiconductors with smaller currents can be employed as well as smaller voltages, taking advantage of the multilevel structure.

Regarding the CHB multilevel converter, several studies have been developed in order to reduce the number of switched components, having as a comparison parameter the same number of voltage levels, minimizing the cost and volume of the converter [31].

In systems with waveforms with low voltage levels, as in the case of the present work, the conventional structure of the CHB multilevel converter does not present a major disadvantage when compared to the recently developed topologies [32].

In order to support the choice of the CHB multilevel converter used in this work, Table 2 presents a summary of the advantages and disadvantages of the most used multilevel converters in the industry.

Table 2. Comparison of multilevel converter topologies.

Multilevel Converter	Advantages	Disadvantage
NPC	<ul style="list-style-type: none"> - Ease of increasing the number of levels [25] - Grid transformer is simple [33] - Bus capacitor is small [33] 	- Need to control the difference between capacitor’s voltages [25]
		- Unequal loss distribution [25]
		- Unsymmetrical semiconductor-junction temperature distribution [25]
		- Limitation on the number of levels [34]

Table 2. Cont.

Multilevel Converter	Advantages	Disadvantage
FC	- Modular structure [25]	- Flying capacitor cost is high for low and medium switching frequency operation [25]
	- Symmetrical semiconductor loss distribution [33]	- High number of cells [25]
	- First carrier frequency band is high [33]	- As levels increase, the number of capacitors increases [34]
CHB	- Modular structure [25]	- Complexity in the control strategy due to capacitor voltage regulation [34]
	- Low switching losses [25]	- Pre-charge of the capacitors, which implies in the decrease of the performance of the system [34]
	- LC filter with smaller components compared to NPC and FC converters [33]	- Separate dc sources [25]
	- First carrier frequency band is high maximum [33]	- Need a phase-shifting transformer in the grid [33]
	- Does not require clamped diodes or flying capacitors [34]	- Bigger DC-link capacitor compared to NPC [33]
	- Reaches higher voltage and higher power levels [4]	- Higher number of switching components [31]

3.1. Modulation Strategy

With multilevel topologies, if on one hand the control of the various switches of the converter has become more complex, on the other hand the possibility of several redundancies of the switching states is one of the advantages, as explained earlier. Different algorithms of modulation techniques have been proposed for multilevel converters [4].

For the system proposed in this work, the phase-shift modulation technique, commonly called PS-PWM, was used. This technique is an extension of the traditional modulation PWM, and is widely used in CHB converters [4]. In this modulation strategy, a phase shift is introduced between the signals of the carriers of contiguous cells and, consequently, the output of the converters has a phased behavior, resulting in a waveform with steps, i.e., a multilevel output. The modularity characteristic of multilevel converters facilitates this modulation strategy, as each cell is modulated independently, using the same reference signal [6].

In order to achieve the lowest possible harmonic distortion in the output, the phase shift between the carriers of adjacent cells (top and bottom cells) must be 180° or $360^\circ/n$ for the CHB and FC converters, respectively, where n is the number of converter cells. Based on Figure 5, the cells of each phase—on the MSC side—will be modulated by PS-PWM and the phase shift between the carriers of the top cells (top) and those of the bottom cells (bottom) is 90° [6].

Figure 6 shows the implementation of PS-PWM for one phase of the CHB employed in this work. For the other phases, the implementations are similar, but the reference voltage ($v_{control}$) is 120° or 240° shifted.

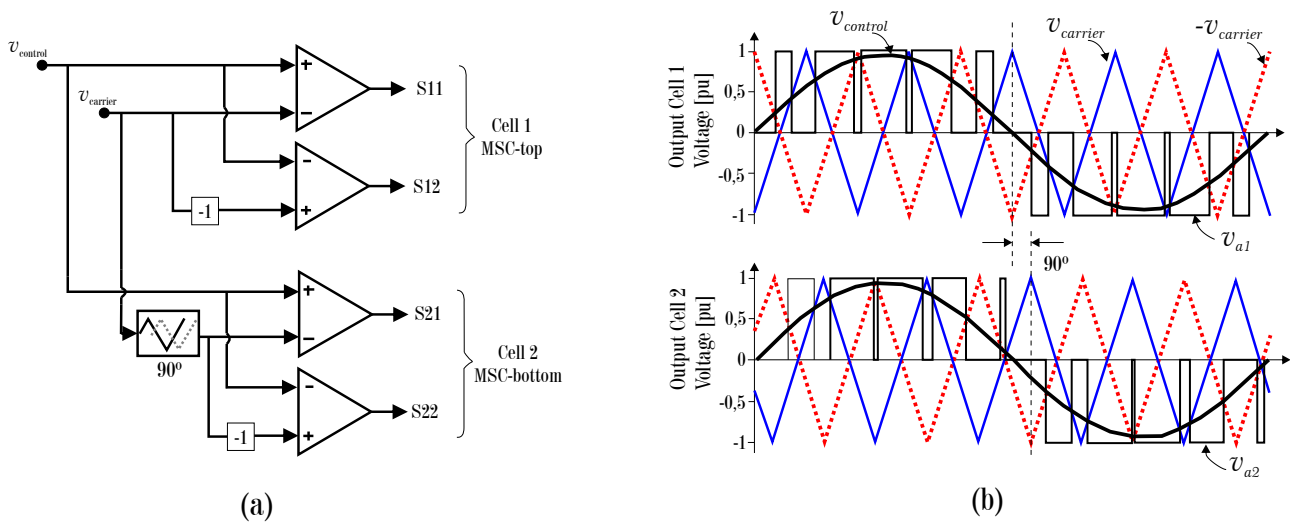


Figure 6. Modulation technique (PS-PWM) used in the switching of CHB multilevel converters. (a) Two-cell (five-level) control diagram for CHB. (b) Reference signal and carriers waveforms for five-level CHB. (Adapted from [6]).

3.2. Control Strategies

As previously mentioned, the GSCs have the function of controlling the DC-link voltages, as well as executing the control of reactive power in the grid. The MSCs are mainly responsible for the maximum power point tracking (MPPT) of the wind turbine and the induction machine magnetization [35].

For machine control, the rotor flux orientation in synchronous reference frame dq is used. This well known technique has the advantage of decoupling the magnetization and the torque of the machine through the direct and quadrature currents, respectively [28,36].

With the rotor flux-oriented control, it is possible, as shown in Equation (13), to vary the machine torque just by controlling the quadrature current of the stator, since $\lambda_{rq} = constant$, which means $i_{sd} = constant$. Combining Equations (6), (9) and (10), it is shown that the machine flux depends on the direct current:

$$\lambda_{rd} = \frac{L_m}{1 + (L_r/R_r)p} i_{sd}. \tag{16}$$

The orientation angle of the synchronous reference frame can be obtained through the slip ratio of the machine. Knowing that $\lambda_{rq} = 0$ and substituting i_{rq} in Equation (9) on Equation (6):

$$(\omega_{sf} - \omega_e) = s\omega_{sf} = \frac{R_r L_m}{L_r \lambda_{rd}} i_{sq}. \tag{17}$$

Therefore, with the control reference signals, λ_{rd}^* (Equation (16)) and i_{sq}^* (Equation (17)), and the measurement of the machine electrical speed (ω_e), the orientation angle can be obtained, as shown in Figure 7, where ω_{sf} is the synchronous speed.

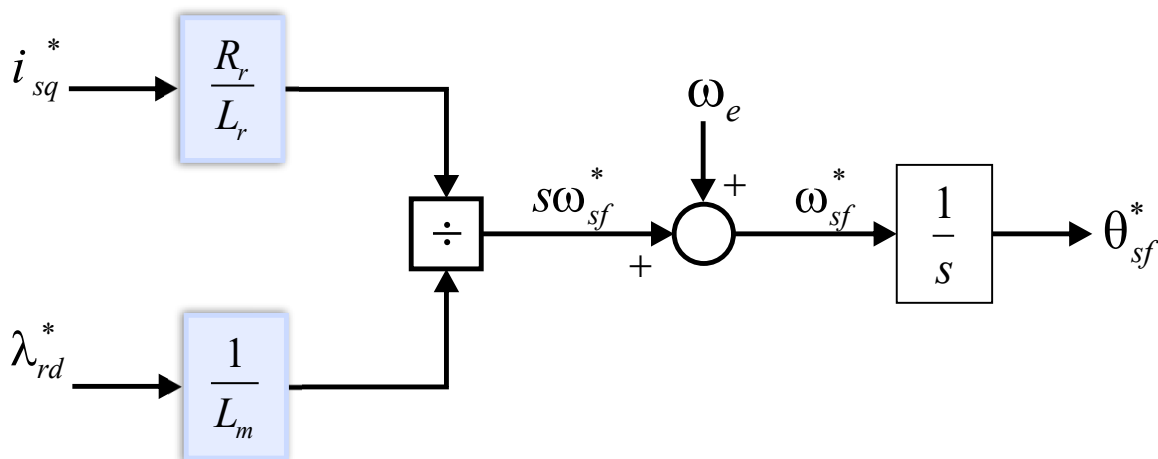


Figure 7. Induction machine rotor flux position estimation for control orientation. (The superscript * refers to reference value).

Figure 8 shows the MSC control loops; as noted, the direct axis current reference (i_{sd}^* , Equation (16)) is calculated from the machine flux (λ_{rd}). Given that the machine flux has stabilized, the flux value will remain constant as long as the system remains below the rated speed. The current required to maintain this flux is:

$$i_{sd}^* = \frac{\lambda_{rd}}{L_m}. \tag{18}$$

The quadrature axis current reference (i_{sq}^*) is related to the electromagnetic torque to be applied to the machine. The torque is related to the speed of the machine, through the maximum power coefficient curve of the wind turbine. The objective is to operate the WECS on the maximum power points of the wind curves. The optimal generator speed (ω_{ref}) is defined as the ratio between the tip speed ratio, the wind speed, and the blade radius [37,38]. Therefore, in Figure 8, the machine reference speed is defined based on the wind speed over the turbine:

$$\omega_{optimal} = \frac{\lambda_{optimal}}{r} V_w. \tag{19}$$

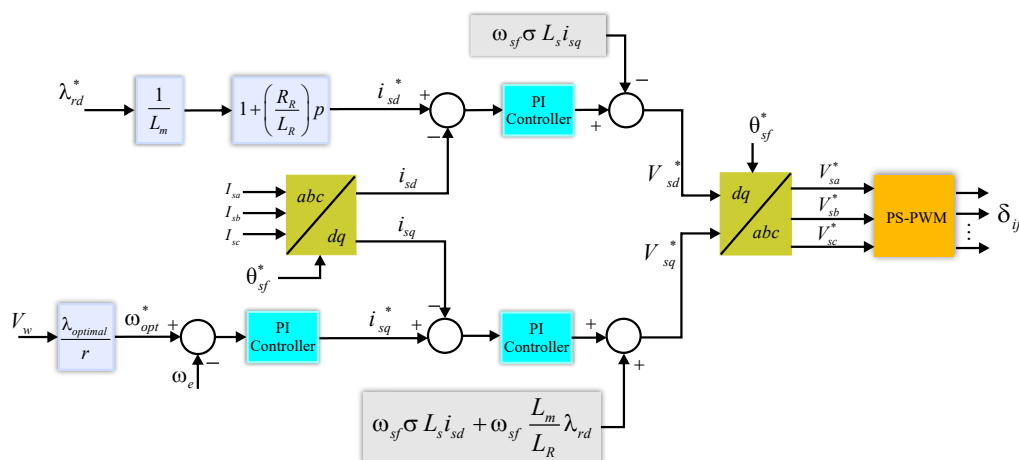


Figure 8. MSC control structure for SCIG. (The superscript * refers to reference value)

In Figure 8, the variables $\sigma = (1 - L_m^2/L_s L_r)$ and δ_{ij} are the semiconductor command pulses.

The compensation terms that appear after adding the PI controller are obtained from the stator voltage equations:

$$v_{sq} = R_s i_{sq} + \sigma L_s p \lambda_{sq} + \omega_{sf} \sigma L_s i_{sd} + \omega_{sf} \frac{L_m}{L_r} \lambda_{rd} \quad (20)$$

$$v_{sd} = R_s i_{sd} + \sigma L_s p \lambda_{sd} - \omega_{sf} \sigma L_s i_{sq} \quad (21)$$

where the compensation terms are:

$$v_{comp,q} = \omega_{sf} \sigma L_s i_{sd} + \omega_{sf} \frac{L_m}{L_r} \lambda_{rd} \quad (22)$$

$$v_{comp,d} = -\omega_{sf} \sigma L_s i_{sq}. \quad (23)$$

As can be seen in Figures 8 and 9, proportional-integral (PI) controllers were employed in both MSC and GSC current control loops. For the tuning of the PI controllers of current control of the MSC, the method called Modulus Optimum (MO) was used, which is commonly used in the tuning of controllers of control systems that involve inverters and electrical machines [39,40]. The equations of the gains are:

$$T_i = \frac{L_{total}}{R_{total}}; \quad K_p = \frac{L_{total}}{2T_{sw}}; \quad K_i = \frac{K_p}{T_i}, \quad (24)$$

where L_{total} and R_{total} are the electrical machine parameters defined by the sum of the leakage inductances (L_s and L_r) and the sum of the resistances of the stator and rotor windings (R_s and R_r), respectively, and T_{sw} is the converter switching period.

The GSC controls are also implemented in the synchronous frame, with orientation angle based on grid voltages. To obtain this angle, the present work uses the SOGI-PLL technique [41]. The equations that describe the dynamic behavior of voltage and current in the grid, in the synchronous reference frame, are:

$$v_{conv,d} = R_T i_d + L_T \frac{di_d}{dt} + v_{grid,d} - \omega L_T i_q \quad (25)$$

$$v_{conv,q} = R_T i_q + L_T \frac{di_q}{dt} + v_{grid,q} + \omega L_T i_d, \quad (26)$$

where $v_{conv,d}$ and $v_{conv,q}$ are the converters voltage; R_T and L_T are the total filter resistance (R_g and R_f) and inductance (L_f and L_g); and ω is the grid angular frequency.

The controls of the mains converters are single-phase, which implies that the control loop of the DC-link is individual for each GSC. Figure 9 shows the current control structures for the grid-side converters. For simplicity, only the phase-A current control loop has been presented, but the controls of the other six converters are identical.

The current control loop of the grid-side converters (GSC) is an internal loop, with faster dynamics; however, the operating frequency of that loop cannot be faster than the switching frequency, otherwise the system will not have enough time to react to a command of that loop. For this reason, it was decided to tune it at a frequency ten times lower than the system's switching frequency. The external DC-link voltage loop was tuned slower (167 times smaller than the current loop) in order to follow the inherent power oscillations coming from the fact that the GSC is in truth three single-phase converters, as shown in Figure 5. As can be seen in the same figure, from the phase current, the second-order generalized integrator-based quadrature signal generator (SOGI-QSG) is used to obtain the currents in the $\alpha\beta$ stationary reference frame.

The DC-link voltage oscillation in single phase converters is a well known problem of this kind of system. The DC capacitor can be increased to reduce the oscillation or this can be treated by the control, as done here. In order to avoid high oscillation of the DC-link voltage, resulting from a harmonic at a frequency of 120 Hz ($2 \cdot \omega$); the measured signal of the DC voltage is filtered using a notch filter tuned at this frequency.

The variables shown in Figure 9 are: L_T is the sum of filter inductances; I_a, I_b, I_c are the grid phase currents; V_{grid} is the voltage grid; $V_{ga,d}$ and $V_{ga,q}$ are the grid voltage in the

synchronous reference frame; ω is the grid angular frequency; Q^* and Q are reactive power reference and measured reactive power, respectively; and finally, V_{dc}^* and V_{dc} are the dc-link voltage reference and measured dc-link voltage, respectively.

At the output of the grid-side converters, LCL filters are connected in order to minimize the harmonic content of the currents flowing into the grid. The design of the LCL filters was developed so that a maximum ripple of 3% occurs in the output current of the converters, following the procedure presented in reference [42].

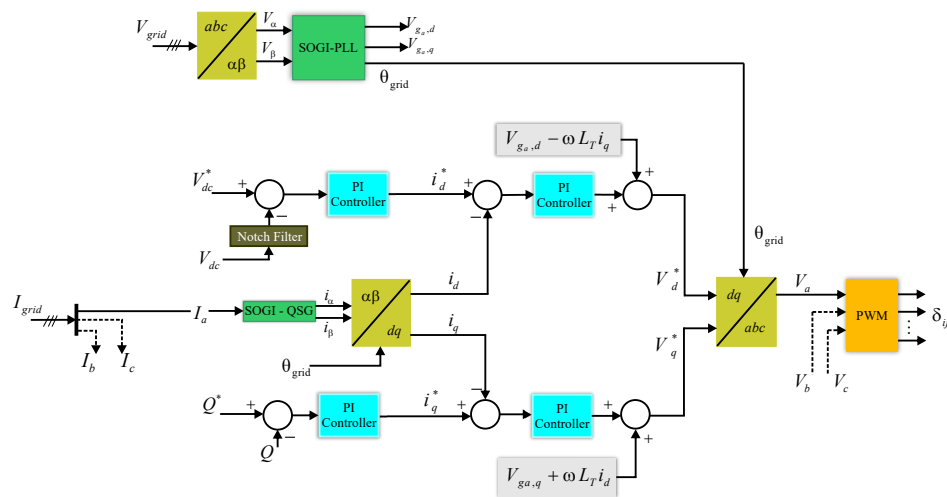


Figure 9. GSC control structure. (The superscript * refers to reference value).

4. Results and Discussion

The simulation carried out in this article is based on five-level back-to-back converters (two three-level converters connected in OEW), as shown in Figure 5, to evaluate the behavior of the proposed system, using PLECS[®] software.

The main parameters of the squirrel-cage induction machine as well as the parameters of the converters and LCL filter are presented in Table 3. The Infineon IGBT power modules chosen for this proposed system were the FZ825R33HE4D module ([43]) for the GSC and the FF450R33T3E3 module ([44]) for the MSC. Both have a blocking voltage of 3300 V and a current capacity of 825 A and 450 A, respectively.

Table 3. Parameters of squirrel-cage induction machine [45], LCL filter and converters.

Parameter	Value
Rated output power	1677 kW
Nominal line stator voltage	2300 V(rms)
Nominal stator current	421.2 A(rms)
Nominal Frequency	60 Hz
Nominal rotor speed	1786 rpm
Number of poles pairs	2
Rated mechanical torque	8.9 kNm
Stator winding resistance, R_s	29 m Ω
Rotor winding resistance, R_r	22 m Ω
Stator leakage reactance, L_{ls}	0.226 m Ω
Rotor leakage reactance, L_{lr}	0.226 m Ω
Magnetization reactance, L_m	13.04 m Ω
Moment of inertia	63.87 kgm ²
Nominal line grid voltage	1150 V(rms)
Nominal grid frequency	60 Hz

Table 3. *Cont.*

Parameter	Value
DC-link Voltage	2100 V
DC-link Capacitance	12 mF
Switching frequency (MSC and GSC)	5 kHz
Converter side inductor, L_f	6.3 mH
Converter side resistor, R_f	23.8 m Ω
Grid side inductor, L_g	0.63 mH
Grid side resistor, R_g	23.8 m Ω
Parallel capacitor, C	10.03 μ F
Damping resistor, R_d	2.52 m Ω

A sequence of tests was performed in the simulation to verify the system behavior and Table 4 presents the stages of the simulation process.

Table 4. Simulation stages of the proposed system.

Description	Time
Start of simulation	0.0 s
Machine magnetization start at	1.2 s
Machine acceleration starts at	1.8 s
Machine reaches the rated speed at	5.0 s
Reduce equivalent to 20% in machine torque at	8.3 s
Increase of approximately 17% in machine torque at	11.3 s
Reactive power injection at	13.0 s

Considering the steps described in Table 4, the first variables to be stabilized were the DC-link voltages of the six single-phase converters (H-bridge). This control is crucial, since the DC-link is responsible for the power flow through the system. Figure 10 shows, after the initial transient, the behavior of the DC-link control. It can be seen in the figure that the bus reached steady state during the machine magnetization period (before 1.8 s). The first oscillation of the bus occurred at the moment of starting the induction generator, in 1.8 s, when a load torque was applied to the machine, resulting from the action of wind on the turbine.

It is noticed that, at around 5 s, the DC-link voltage oscillates again, because in this moment the machine reaches its nominal speed. At 8.3 s, there is a torque variation on the generator, representing an abrupt wind variation in the turbine. The detail in Figure 10b shows the maximum oscillation on the DC-link, approximately equal to 3% of the DC nominal value. All the other DC-link voltages present the same behavior, and will be not shown.

After the initial transient of the DC-link, the magnetization of the machine started and, during this period, the direct axis current increased until it reached its nominal value, as shown in Figure 11a. After that, the magnetization of the machine kept constant. In Figure 11b, it can be seen that the behavior of the quadrature current followed the behavior of machine torque. In the instants between 8 and 11 s, there was an abrupt variation in the wind speed, which implied variations in torque of the machine, and such variations were also observed in the quadrature current. In both cases, the direct and quadrature currents followed the reference accordingly.

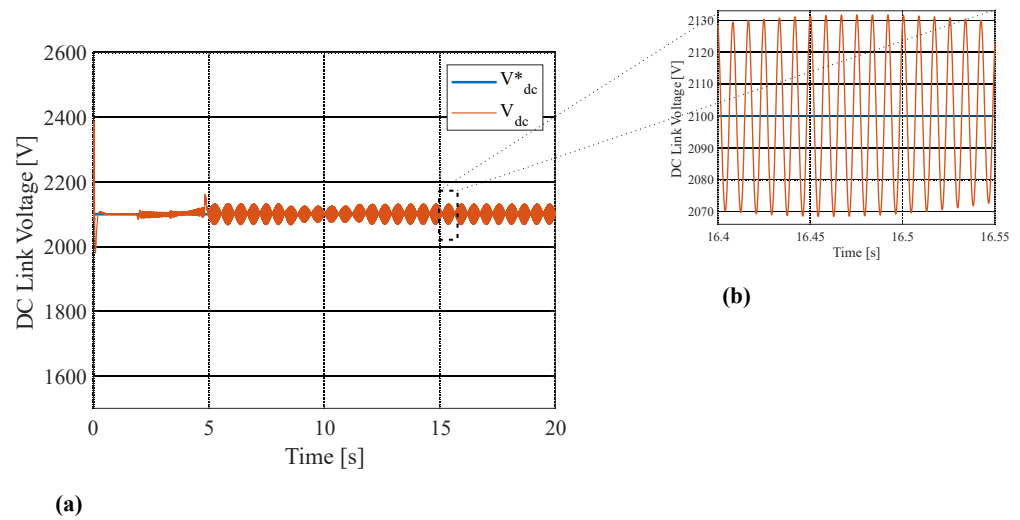


Figure 10. Behavior of the DC-link voltage, where V_{dc}^* refers to DC-link voltage reference, while V_{dc} is the measured value. (a) DC-link voltage phase A. (b) Detail, zoomed in, showing the maximum oscillation of the DC-link voltage.

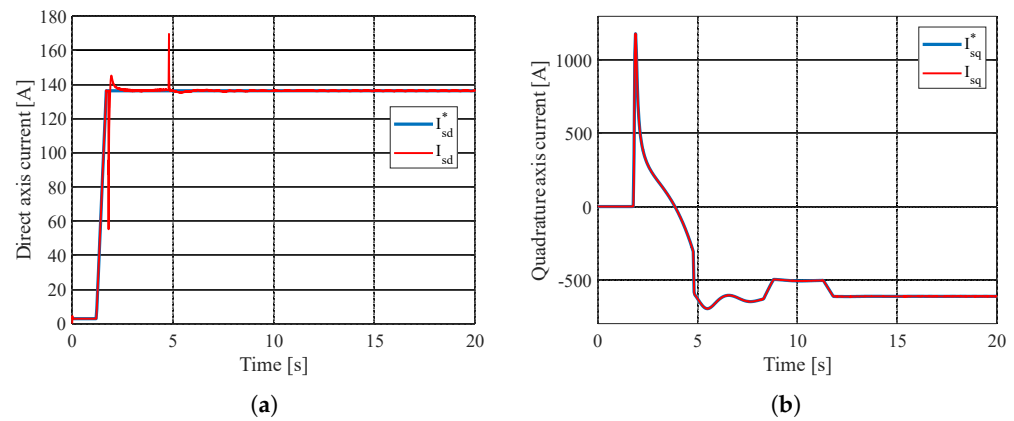


Figure 11. Machine side–converter currents, where I_{sd}^* and I_{sq}^* are the direct and quadrature current reference; I_{sd} and I_{sq} are the measured value. (a) Direct axis component. (b) Quadrature axis component.

After the machine was magnetized, it was allowed to accelerate up to rated speed. Next, in Figure 12, the behavior of the generator speed is shown. It is seen that the generator speed followed the reference well. In this case, the variation of speed was simulated from standstill until the rated speed (rated power extraction) was reached. It is noticeable that, even during the abrupt torque variation (detail of Figure 13), relevant variation in machine speed was not observed.

With the machine operating in a steady state, load torques were applied in order to simulate the action of winds on the turbine. Figure 13 shows the behavior of the turbine torque, and the detail of the same figure shows the abrupt variation at the instant of time 8.3 s and, around 11.3 s, the torque returns to approximately 97% of the nominal value. In the simulation, the dynamics of the wind turbine was not considered, thus, an abrupt torque variation was analyzed to verify the control behavior. Additionally, Figure 13 shows the electromagnetic torque of the machine, varying according to the turbine torque and acceleration. The positive torque means generation and the torque was negative during the transient acceleration to reach the maximum wind power extraction.

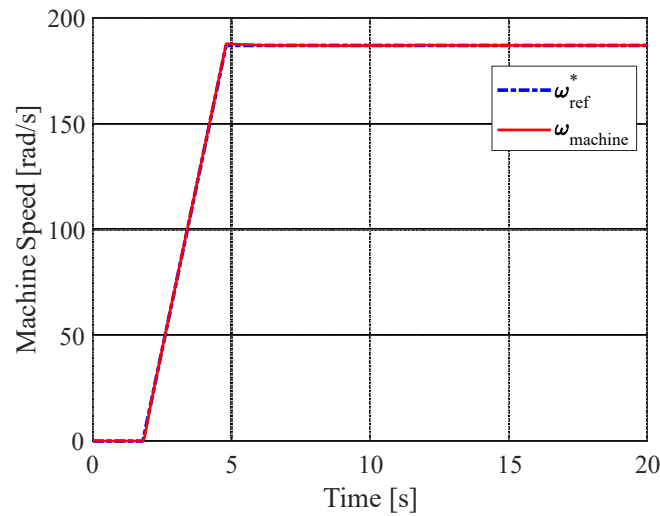


Figure 12. Machine speed, where the reference value is ω_{ref}^* and the measured value is $\omega_{machine}$.

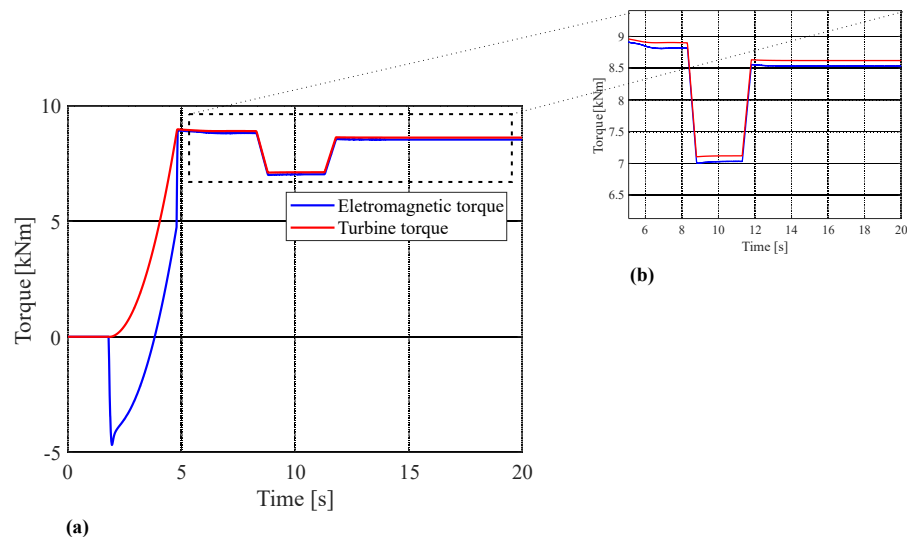


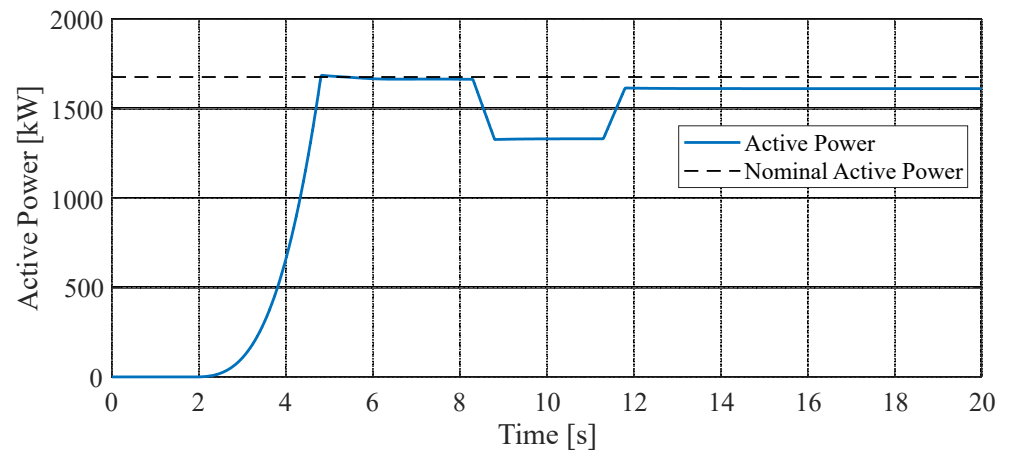
Figure 13. Turbine and machine electromagnetic torques. (a) Behavior of torques throughout the simulation. (b) Detail, zoomed in, showing abrupt variation in wind speed, reflecting on turbine torque and, consequently, on electromagnetic torque.

The behavior of the generator shaft power can be seen in Figure 14a; as the generator received the turbine torque, the power started to be delivered until it reached its nominal value of approximately 1.677 MW. The same analysis developed on the load torque can be performed here as well, where the abrupt variation in power due to the change in machine torque was seen.

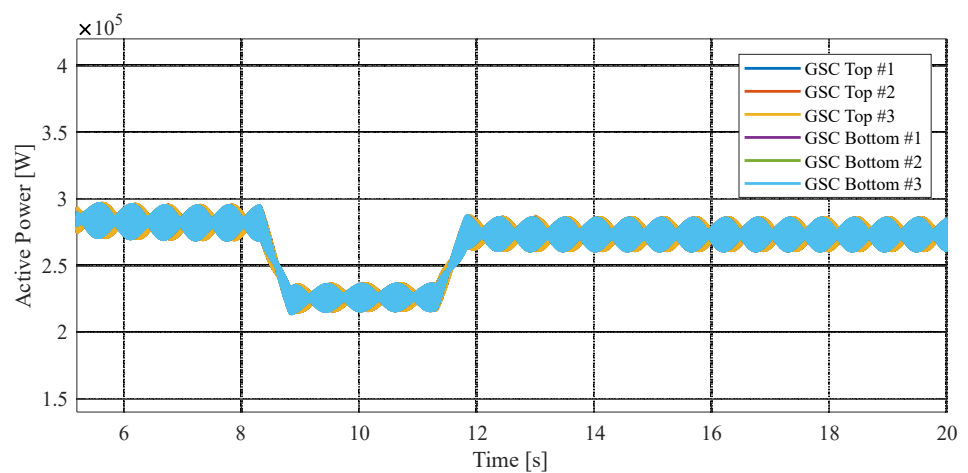
Figure 14b presents the active power delivered by each of the six converters (GSC) implemented in the proposed system. It was noticed that there was distribution of the power between them, since each one delivered approximately 0.280 MW to the grid, when operating at nominal power. This power distribution is one of the advantages of this system, because individual converters with smaller powers can be employed. Furthermore, if one or more converters fail, it is possible to continue the operation (operation under faults is out of the scope of the present paper). The oscillations in this power are due to the single phase connection to the grid.

The same analysis can be performed in terms of the reactive power supplied to the grid. Figure 15 shows the behavior of the reactive power control loop, phase A, when a step is applied to the power reference. By analyzing the response to step variation in reactive power, it is possible to verify that the rise time is approximately 0.18 s with an overshoot of 7.5%. The oscillation seen at the output of the converter was again due to the single phase connection of each converter. Considering all converters, this oscillation was in the range of 2% in relation to the reference reactive power. All other reactive powers delivered by the converters presented the same behavior, and will not be shown.

Figure 16a shows the voltage synthesized at the terminals of the induction machine due to the operation of the converters. As seen, the synthesized voltage was five-level, with a peak value equal to 4200 V ($2V_{dc}$). The semiconductors employed in each converter need to support V_{dc} (2100 V), instead of $2V_{dc}$ (4200 V), therefore the IGBT blocking voltage can be 3300 V, as stated previously. In the same way, Figure 16b presents the current at the machine terminals.



(a)



(b)

Figure 14. Active power in generator and converters. (a) Behavior of total active power throughout the simulation. (b) Distribution of active power among GSC.

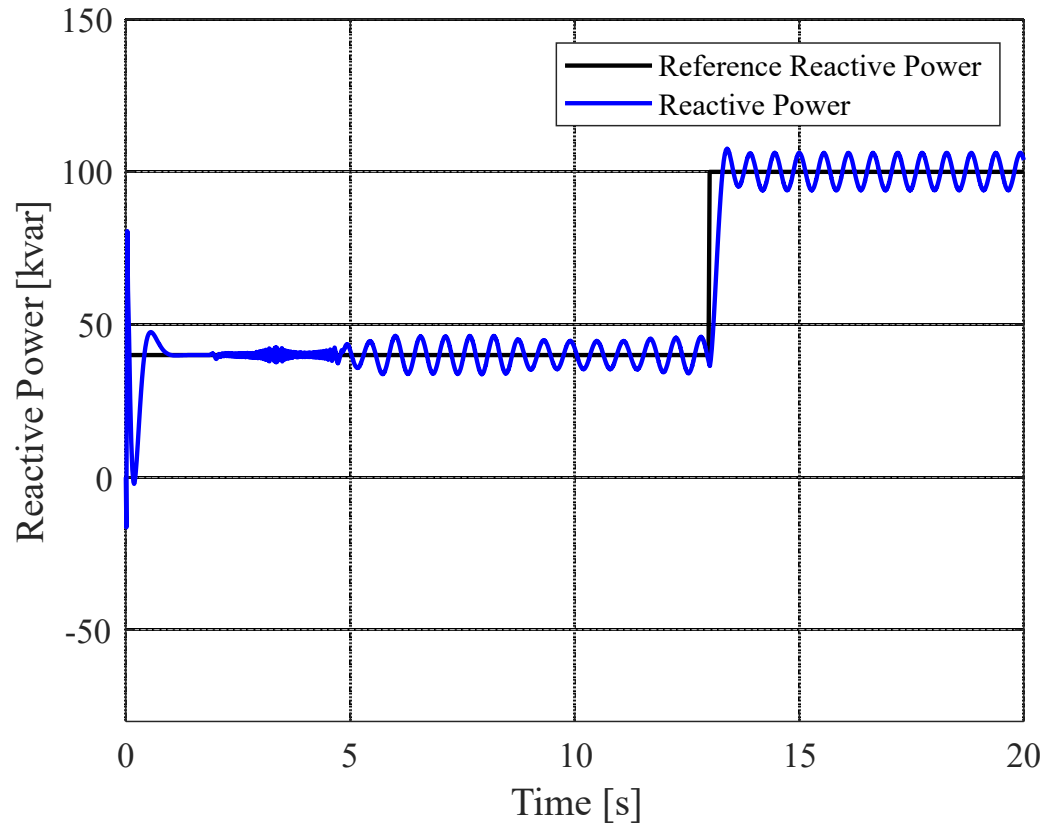


Figure 15. Reactive power, phase A, in a proposed WECS.

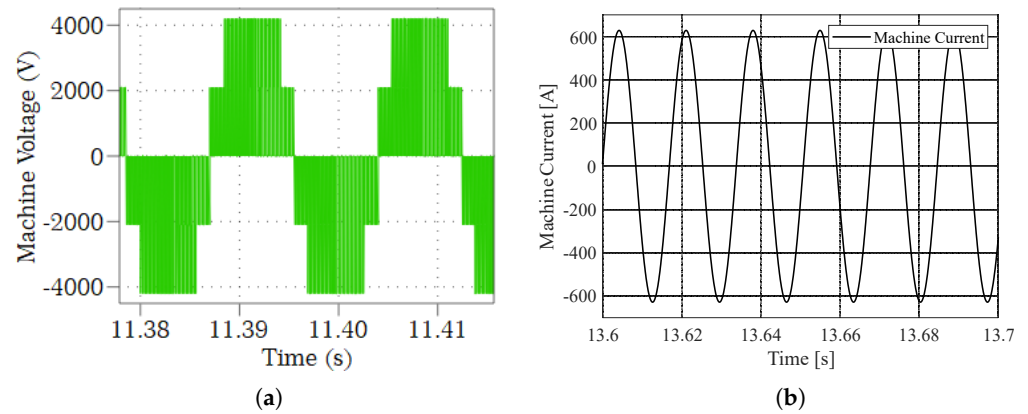


Figure 16. Machine voltage and currents. (a) Machine Voltage. (b) Machine Currents.

Figure 17a shows the behavior of the grid currents and the consequences of variations in machine torque and power can be seen in the behavior of the currents. Furthermore, the graph shown in Figure 17b shows, in detail, the grid currents, which have a sinusoidal waveform with small harmonic distortion.

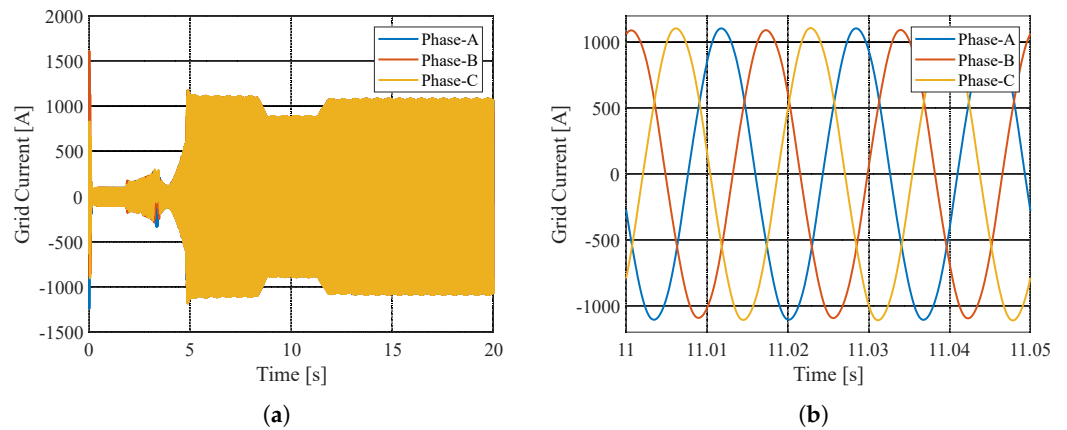


Figure 17. Grid currents. (a) Grid currents throughout the simulation. (b) Grid currents in detail.

An important analysis to be performed on the current obtained at the machine terminals and grid current was the harmonic spectrum of these components. Figure 18 shows the harmonic spectrum of the current at the machine terminals. The machine current $THD_{i,mach}$ was about 4.05%. Figure 19 shows the harmonic spectrum of the grid current, showing the small harmonic distortion attained. The $THD_{i,grid}$ value of the grid current was 0.69%. Both THDs were relatively low, proving another advantage of using multilevel converters.

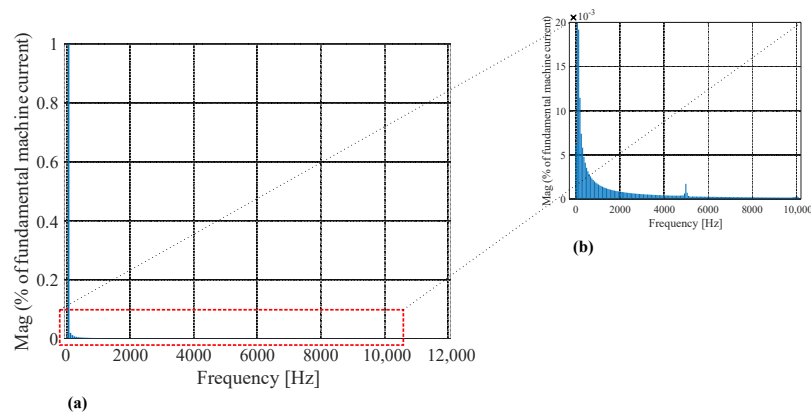


Figure 18. Harmonic spectrum of machine current. (a) Overview of the harmonic content of currents at the machine terminals. (b) Detail, in zoom, showing the low harmonic content in currents of the machine.

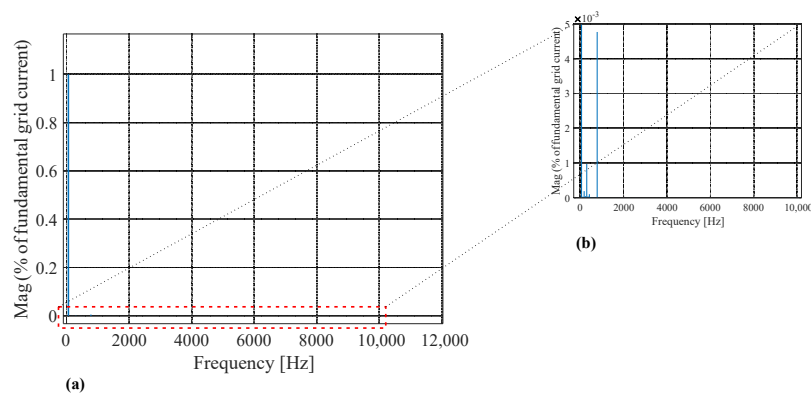


Figure 19. Harmonic spectrum of grid current. (a) Overview of the harmonic content of the currents at the grid. (b) Detail, zoomed in, showing the lowest harmonic content in currents flowing in the grid.

5. Conclusions

In this work, a squirrel-cage induction machine drive was presented in an open-end windings configuration, supplied by a five-level back-to-back converter, in a CHB multilevel topology. The proposed work was based on a wind energy conversion system. The PS-PWM modulation technique used in this system allowed it to present a good performance with regard to the low harmonic content in the machine currents, whose $THD_{i,mach}$ value was approximately equal to 4%. After the designed LCL filter, the currents in the grid presented harmonic content lower than 1% ($THD_{i,grid}$ around 0.7%).

The great advantage in the development of multilevel converters is the modularity, reliability and redundancy in the switching states. It can be seen that the proposed system was carried out within what was expected, that is, the voltage synthesized at the machine terminals was five-level and low current THD value. The good performance of the control loops can also be seen in the response time of the reactive power loop, which is approximately 0.18 s, with an overshoot of around 7.5%.

The implemented control also demonstrated a good performance. The machine speed was controlled without overshoots and following the references even during abrupt turbine torque variations. During such variations, the DC-link voltage was also well controlled, permitting the delivery of power to the grid. This can be seen in the low value of the oscillation present in the measured DC-link voltage, which in a steady state is approximately equal to 3% of its nominal value.

Future work will include obtaining experimental results on a prototype of a low-power WECS, under development. Furthermore, strategies to operate the system under converter fails will be investigated, in order to take advantage of the multi converter structure.

Author Contributions: Conceptualization, V.F.M. and F.F.M.; methodology, V.F.M. and F.F.M.; validation, S.d.S.B.; formal analysis, S.d.S.B., H.d.O.R. and V.F.M.; investigation, S.d.S.B.; resources, S.d.S.B.; writing—original draft preparation, S.d.S.B.; writing—review and editing, H.d.O.R. and V.F.M.; supervision, V.F.M. All authors have read and agreed to the published version of the manuscript.

Funding: This work has been supported by the Coordination for the Improvement of Higher Education Personnel-Brazil (CAPES)-Financing Code 001, the National Council for Scientific and Technological Development (CNPQ) project 408059/2021-4 and the Minas Gerais Research Funding Foundation (FAPEMIG) project APQ-01187-18.

Institutional Review Board Statement: Not applicable.

Informed Consent Statement: Not applicable.

Data Availability Statement: Request from the authors.

Conflicts of Interest: The authors declare no conflict of interest.

Abbreviations

The following abbreviations are used in this manuscript:

CHB	Cascaded H-Bridge
FC	Flying Capacitor
GSC	Grid-side Converter
MSC	Machine-side Converter
NPC	Neutral Point Clamped
OEW	Open-end Winding
SCIM	Squirrel-Cage Induction Machine
WECS	Wind Energy Conversion System

References

1. GWEC. Global Wind Report 2022. Available online: <https://gwec.net/wp-content/uploads/2022/03/GWEC-GLOBAL-WIND-REPORT-2022.pdf> (accessed on 16 January 2023).
2. REN21. Renewables 2022 Global Status Report. Available online: https://www.ren21.net/wp-content/uploads/2019/05/GSR2022_Full_Report.pdf (accessed on 16 January 2023).
3. Franquelo, L.G.; Rodriguez, J.; Leon, J.I.; Kouro, S.; Portillo, R.; Prats, M.A. The age of multilevel converters arrives. *IEEE Ind. Electron. Mag.* **2008**, *2*, 28–39. [[CrossRef](#)]
4. Kouro, S.; Malinowski, M.; Gopakumar, K.; Pou, J.; Franquelo, L.G.; Wu, B.; Rodriguez, J.; Pérez, M.A.; Leon, J.I. Recent advances and industrial applications of multilevel converters. *IEEE Trans. Ind. Electron.* **2010**, *57*, 2553–2580. [[CrossRef](#)]
5. Ma, K.; Blaabjerg, F. Multilevel converters for 10 MW wind turbines. In Proceedings of 2011-14th European Conference on Power Electronics and Applications (EPE 2011), Birmingham, UK, 30 August–1 September 2011; pp. 1–10.
6. Rodriguez, J.; Franquelo, L.G.; Kouro, S.; Leon, J.I.; Portillo, R.C.; Prats, M.A.M.; Perez, M.A. Multilevel converters: An enabling technology for high-power applications. *Proc. IEEE* **2009**, *97*, 1786–1817. [[CrossRef](#)]
7. Nabae, A.; Takahashi, I.; Akagi, H. A New Neutral-Point-Clamped PWM Inverter. *IEEE Trans. Ind. Appl.* **1981**, *IA-17*, 518–523. [[CrossRef](#)]
8. Meynard, T.A.; Foch, H. Multi-Level Choppers for High Voltage Applications. *Epe J.* **1992**, *2*, 45–50. [[CrossRef](#)]
9. Kedika, N.R.; Pradabane, S. Fault-tolerant multi-level inverter topologies for open-end winding induction motor drive. *Int. Trans. Electr. Energy Syst.* **2021**, *31*, 12718. [[CrossRef](#)]
10. Marchesoni, M.; Mazzucchelli, M.; Tenconi, S. A non conventional power converter for plasma stabilization. In Proceedings of the PESC '88 Record, 19th Annual IEEE Power Electronics Specialists Conference, Kyoto, Japan, 11–14 April 1988; Volume 1; pp. 122–129. [[CrossRef](#)]
11. Osman, R. A medium-voltage drive utilizing series-cell multilevel topology for outstanding power quality. In Proceedings of the Conference Record of the 1999 IEEE Industry Applications Conference. Thirty-Forth IAS Annual Meeting (Cat. No.99CH36370), Phoenix, AZ, USA, 3–7 October 1999; Volume 4; pp. 2662–2669. [[CrossRef](#)]
12. Blaabjerg, F.; Liserre, M.; Ma, K. Power Electronics Converters for Wind Turbine Systems. *IEEE Trans. Ind. Appl.* **2012**, *48*, 708–719. [[CrossRef](#)]
13. Ma, K.; Blaabjerg, F.; Xu, D. Power devices loading in multilevel converters for 10 MW wind turbines. In Proceedings of the 2011 IEEE International Symposium on Industrial Electronics, Gdansk, Poland, 27–30 June 2011; pp. 340–346. [[CrossRef](#)]
14. Pires, V.F.; Foito, D.; Silva, J.F. Fault-Tolerant Multilevel Topology Based on Three-Phase H-Bridge Inverters for Open-End Winding Induction Motor Drives. *IEEE Trans. Energy Convers.* **2017**, *32*, 895–902. [[CrossRef](#)]
15. Stemmler, H.; Guggenbach, P. Configurations of high-power voltage source inverter drives. In Proceedings of the Fifth European Conference on Power Electronics and Applications, Brighton, UK, 13–16 September 1993; Volume 5; pp. 7–14.
16. Hong, J.; Lee, H.; Nam, K. Charging Method for the Secondary Battery in Dual-Inverter Drive Systems for Electric Vehicles. *IEEE Trans. Power Electron.* **2015**, *30*, 909–921. [[CrossRef](#)]
17. Jain, S.; Thopukara, A.K.; Karampuri, R.; Somasekhar, V.T. A Single-Stage Photovoltaic System for a Dual-Inverter-Fed Open-End Winding Induction Motor Drive for Pumping Applications. *IEEE Trans. Power Electron.* **2015**, *30*, 4809–4818. [[CrossRef](#)]
18. Rajeevan, P.P.; Sivakumar, K.; Gopakumar, K.; Patel, C.; Abu-Rub, H. A Nine-Level Inverter Topology for Medium-Voltage Induction Motor Drive With Open-End Stator Winding. *IEEE Trans. Ind. Electron.* **2013**, *60*, 3627–3636. [[CrossRef](#)]
19. Somasekhar, V.; Baiju, M.; Mohapatra, K.; Gopakumar, K. A multilevel inverter system for an induction motor with open-end windings. In Proceedings of the IEEE 2002 28th Annual Conference of the Industrial Electronics Society. IECON 02, Seville, Spain, 5–8 November 2002; Volume 2; pp. 973–978. [[CrossRef](#)]
20. Matos, F.F.V.; Ramos, H.d.O.; Rocha, D.C.G.; da Silva, R.M.; Mendes, M.A.S.; Mendes, V.F. A multilevel wind power conversion system with an open winding squirrel cage induction generator. In Proceedings of the 2015 IEEE 13th Brazilian Power Electronics Conference and 1st Southern Power Electronics Conference (COBEP/SPEC), Fortaleza, Brazil, 29 November–2 December 2015, pp. 1–6. [[CrossRef](#)]
21. Ricardi, V.; Ferreira Viana Matos, F.; Rodrigues de Jesus, V.M.; de Sousa, C.V.; de Almeida Zica, L.E.L.; Mendes, V.F. Control and operation of open-end winding permanent magnet synchronous wind generator. In Proceedings of the 2017 Brazilian Power Electronics Conference (COBEP), Luiz de Fora, Brazil, 19–22 November 2017; pp. 1–6. [[CrossRef](#)]
22. Vattuone, L.; Kouro, S.; Estay, G.; Wu, B. Open-end-winding PMSG for wind energy conversion system with dual boost NPC converter. In Proceedings of the 2013 IEEE International Conference on Industrial Technology (ICIT), Cape Town, South Africa, 25–28 February 2013; pp. 1763–1768. [[CrossRef](#)]
23. Xing, N.; Hu, S.; Lin, Z.; Tan, Z.; Cao, W.; Gadoue, S. New Adaptive Control Strategies for Open-End Winding Permanent Magnet Synchronous Generator (OEW-PMSG) for Wind Power Generation. In Proceedings of the The 10th International Conference on Power Electronics, Machines and Drives (PEMD 2020), Virtual, 15–17 December 2020; Volume 2020; pp. 838–843. [[CrossRef](#)]
24. Matos, F.F.; Mendes, M.A.; Meynard, T.; Mendes, V.F. A generalized open-end winding conversion system using flying capacitor cells. *Electr. Power Syst. Res.* **2019**, *169*, 174–183. [[CrossRef](#)]
25. Rodríguez, J.; Bernet, S.; Wu, B.; Pontt, J.O.; Kouro, S. Multilevel voltage-source-converter topologies for industrial medium-voltage drives. *IEEE Trans. Ind. Electron.* **2007**, *54*, 2930–2945. [[CrossRef](#)]
26. Teodorescu, R.; Liserre, M.; Rodríguez, P. *Grid Converters for Photovoltaic and Wind Power Systems*; Wiley: London, UK, 2011.

27. Orłowska-Kowalska, T.; Blaabjerg, F.; Rodríguez, J. *Advanced and Intelligent Control in Power Electronics and Drives*; Springer: Cham, Switzerland, 2014.
28. Vas, P. *Vector Control of AC Machines*; Oxford University Press: Cary, NC, USA, 1990.
29. Jacobina, C.B.; Rocha, N.; Marinus, N.S.M.L. Open-end winding permanent magnet synchronous generator system with reduced controlled switch count. In Proceedings of the 2013 Brazilian Power Electronics Conference, Gramado, Brazil 27–31 October 2013; pp. 692–698. [\[CrossRef\]](#)
30. Sivakumar, K.; Das, A.; Ramchand, R.; Patel, C.; Gopakumar, K. A three level voltage space vector generation for open end winding IM using single voltage source driven dual two-level inverter. In Proceedings of the TENCON 2009—2009 IEEE Region 10 Conference, Singapore, 23–26 November 2009; pp. 1–5. [\[CrossRef\]](#)
31. Darvish Falehi, A. Half-cascaded multilevel inverter coupled to photovoltaic power source for AC-voltage synthesizer of dynamic voltage restorer to enhance voltage quality. *Int. Numer. Model. Electron. Networks, Devices Fields* **2021**, *34*, e2883. [\[CrossRef\]](#)
32. Farakhor, A.; Reza Ahrabi, R.; Ardi, H.; Najafi Ravadanegh, S. Symmetric and asymmetric transformer based cascaded multilevel inverter with minimum number of components. *IET Power Electron.* **2015**, *8*, 1052–1060. [\[CrossRef\]](#)
33. Fazel, S.S.; Bernet, S.; Krug, D.; Jalili, K. Design and comparison of 4-kV neutral-point-clamped, flying-capacitor, and series-connected H-bridge multilevel converters. *IEEE Trans. Ind. Appl.* **2007**, *43*, 1032–1040. [\[CrossRef\]](#)
34. Rabiul Islam, M.; Mahfuz-Ur-Rahman, A.M.; Muttaqi, K.M.; Sutanto, D. State-of-the-Art of the Medium-Voltage Power Converter Technologies for Grid Integration of Solar Photovoltaic Power Plants. *IEEE Trans. Energy Convers.* **2019**, *34*, 372–384. [\[CrossRef\]](#)
35. Blaabjerg, F.; Chen, Z. Power electronics for modern wind turbines. *Synth. Lect. Power Electron.* **2005**, *1*, 1–68.
36. Novotny, D.; Lipo, T. Vector Control and Dynamics of AC Drives. In *Monographs in Electrical and Electronic Engineering*; Clarendon Press: Oxford, UK, 1996; Volume 41.
37. Xia, Y.; Ahmed, K.H.; Williams, B.W. Wind Turbine Power Coefficient Analysis of a New Maximum Power Point Tracking Technique. *IEEE Trans. Ind. Electron.* **2013**, *60*, 1122–1132. [\[CrossRef\]](#)
38. Heier, S. *Grid Integration of Wind Energy: Onshore and Offshore Conversion Systems*; Wiley: Hoboken, NJ, USA, 2014.
39. Suul, J.A.; Molinas, M.; Norum, L.; Undeland, T. Tuning of control loops for grid connected voltage source converters. In Proceedings of the 2008 IEEE 2nd International Power and Energy Conference, Johor Bahru, Malaysia, 1–3 December 2008; pp. 797–802. [\[CrossRef\]](#)
40. Mendes, V.F.; de Sousa, C.V.; Silva, S.; Rabelo, B.C.; Hofmann, W. Modeling and Ride-Through Control of Doubly Fed Induction Generators During Symmetrical Voltage Sags. *IEEE Trans. Energy Convers.* **2011**, *26*, 1161–1171. [\[CrossRef\]](#)
41. Rodríguez, P.; Teodorescu, R.; Candela, I.; Timbus, A.V.; Liserre, M.; Blaabjerg, F. New positive-sequence voltage detector for grid synchronization of power converters under faulty grid conditions. In Proceedings of the 2006 37th IEEE Power Electronics Specialists Conference, Jeju, Republic of Korea, 18–22 June 2006; pp. 1–7. [\[CrossRef\]](#)
42. Peña-Alzola, R.; Liserre, M.; Blaabjerg, F.; Ordonez, M.; Yang, Y. LCL-Filter Design for Robust Active Damping in Grid-Connected Converters. *IEEE Trans. Ind. Inform.* **2014**, *10*, 2192–2203. [\[CrossRef\]](#)
43. Infineon. Datasheet of Module FZ825R33HE4D. Available online: https://www.infineon.com/dgdl/Infineon-FZ825R33HE4D-DataSheet-v01_30-EN.pdf?fileId=5546d46278d64ffd0178f97d4dd50584 (accessed on 15 February 2023).
44. Infineon. Datasheet of Module FF450R33T3E3. Available online: https://www.infineon.com/dgdl/Infineon-FF450R33T3E3-DataSheet-v01_20-EN.pdf?fileId=5546d46254bdc4f50154c8080a4e59f5 (accessed on 15 February 2023).
45. Paul C. Krause, O.W.; Sudhoff, S.D. *Analysis of Electric Machinery and Drive Systems*; IEEE Press Series on Power Engineering; Wiley: Hoboken, NJ, USA, 2002.

Disclaimer/Publisher’s Note: The statements, opinions and data contained in all publications are solely those of the individual author(s) and contributor(s) and not of MDPI and/or the editor(s). MDPI and/or the editor(s) disclaim responsibility for any injury to people or property resulting from any ideas, methods, instructions or products referred to in the content.